Reaching the Fundamental Limitation in CO_2 Reduction to CO with Single Atom Catalysts

Saurav Ch. Sarma,[a±] Jesús Barrio,[b,a±] Alexander Bagger,[a] Angus Pedersen,[b,a] Mengjun Gong,[c] Hui Luo, [a] Mengnan Wang, [b,a] Silvia Favero, [b] Chang-Xin Zhao,[d] Qiang Zhang,[d] Anthony Kucernak,[c] Maria-Magdalena Titirici,[a,e*] Ifan E. L. Stephens.[b*]

a. Department of Chemical Engineering, Imperial College London, SW7 2AZ, London, UK
b. Department of Materials, Royal School of Mines, Imperial College London, SW7 2AZ London, UK
c. Department of Chemistry, Molecular Sciences Research Hub, Imperial College London, White City Campus W12 0BZ London, UK
d. Department of Chemical Engineering, Tsinghua University, 1 Tsinghua Road, Beijing 100084, P.R. China
e. Advanced Institute for Materials Research (WPI-AIMR), Tohoku University, 2-1-1 Katahira, Aobaku, Sendai, Miyagi980-8577, Japan

Email: m.titirici@imperial.ac.uk, i.stephens@imperial.ac.uk**.**

Abstract

The electrochemical CO_2 reduction reaction (CO2RR) to value-added chemicals with renewable electricity is a promising method to decarbonise parts of the chemical industry. Recently, single metal atoms in nitrogen-doped carbon (MNC) have emerged as potential electrocatalysts for CO2RR to CO with high activity and faradaic efficiency, although the reaction limitation for CO2RR to CO is unclear. To understand the comparison of intrinsic activity of different MNCs, we synthesized two catalysts through a decoupled two-step synthesis approach of high temperature pyrolysis and low temperature metalation (Fe or Ni). The highly meso-porous structure resulted in the highest reported electrochemical active site utilisation based on *in situ* nitrite stripping; up to 59±6% for NiNC. *Ex-situ* X-ray absorption spectroscopy confirmed the penta-coordinated nature of the active sites. The catalysts are amongst the most active in the literature for CO_2 reduction to CO. Our density functional theory calculations (DFT) show that their binding to the reaction intermediates approximates to that of Au surfaces. However, we find that the TOFs of the most active catalysts for CO evolution converge, suggesting a fundamental ceiling to the catalytic rates.

Introduction

Rising living standards, thriving industries, and increased transportation in emerging and developed economies have resulted in a record-high energy demand, which is mostly met by the combustion of fossil fuels. As a result, CO_2 emissions from fossil fuels are causing a severe environmental crisis and a threat to social development. Electrocatalytic CO_2 (CO2RR) reduction has emerged as a viable and potential transformative technology to close the carbon cycle. Although the production of hydrocarbons (methanol, ethanol, ethylene etc.) through CO2RR is still challenging in terms of selectivity and efficiency,[1–3] such products can be obtained through a tandem system where CO_2 is reduced to CO, and CO subsequently employed as a renewable feedstock for the Fischer–Tropsch reaction or further electrochemically converted to multi-carbon products.[4,5] CO_2 reduction to CO involves only two electrons and two proton transfers; the state of the art catalysts for the reaction are based on Au and Ag.[6,7], first reported by Hori and coworkers.[8]

Single-metal atom catalysts anchored on porous nitrogen-doped carbon (MNC) have emerged as promising CO_2 electrocatalysts for CO production, owing to their high activity, abundant source materials, high porosity, high conductivity, and potential for 100 % active site utilisation arising from their atomic dispersion.[9–11] Varela *et al*. first reported that Fe/Mn-N_4 sites embedded in graphene can reduce CO_2 to CO.[9] Since their seminal report, many strategies have been used to date for improving selectivity and current density in MNC materials, including tuning the intrinsic activity, enhancing the number of M-N_x sites or controlling the rate of CO_2 diffusion.[12] While plenty of efforts have been dedicated to exploring different metal coordination environments in carbon-based supports,[13–15] the current synthetic protocols for MNC CO_2 electrocatalysts display several drawbacks that hinder intrinsic catalytic activity, selectivity and active site utilisation. MNC catalysts are often prepared by pyrolysis at high temperatures of a mixture comprising a metallic precursor and carbon and nitrogen containing monomers or polymers. With increased metal loadings, such synthetic protocols often lead to the formation of metal nanoparticles, metal oxides and metal carbides, which are active towards hydrogen evolution.[16] Although, in principle, single atom MNC catalysts could exhibit 100% active site utilisation (defined as the electrochemically accessible metal or metal-nitrogen sites compared to the total amount[17,18]), O_2 reduction literature shows that microporous FeNC catalysts often only utilise <10% of atomic active sites.[19,20] However, very recently we reported a synthetic protocol to prepare highly electrochemically accessible FeNC single atom catalysts (FeN_x electrochemical utilisation >50%) employing a decoupled two-step synthesis that entailed low temperature metalation of a templated micro- and mesoporous catalyst.[21]

Despite the continuous effort towards improving the catalyst material, the fundamental origin of the high overpotential in most CO evolution catalysts remains under debate.[22] Electroreduction of CO_2 to CO proceeds through activation of CO_2 and release of CO. Earlier works modelled the activation of CO_2 as a proton coupled electron transfer step to form *COOH.[23,24]. However, more recent studies revealed that CO_2 reduction kinetics are constant on the absolute potential scale versus SHE, independent of pH, both on metals and MNC catalysts, suggesting that CO_2 is activated via an electron transfer uncoupled to proton transfer, potentially involving stabilisation via a cation.[24–26] Nonetheless, the initial activation of CO_2 is easier at more carbophilic catalytic sites (e.g. can be measured as a stronger binding of the *COOH intermediates). However, the second step forming *CO and its subsequent desorption, is better catalysed by less carbophilic catalytic site (e.g. a weaker binding of *CO or *COOH). The scaling relationship between both the C-binding species (*CO and *COOH) leads to a Sabatier volcano. Even at the peak of the volcano, metal catalysts exhibit a substantial overporential.[23] Furthermore, Nitopi *et al*. showed that when compared in terms of intrinsic activity, the most active metal-based catalysts tend to converge towards the activity of pure Cu.[27]

In MNC catalysts, the activity and binding energies can be tuned through the modification of the metal and the coordination environment. Previous studies have reported the trend of CO adsorption energy on FeN_x in the following order (from strong to weak) FeN_2 > FeN_3 > FeN_4 > FeN_5.[28,29] The axial position of a planar Fe-N_4 can be coordinated to any non-metal such as carbon, nitrogen, oxygen or sulphur, thus breaking the site-symmetry and electronic distribution.[30] However, it is not clear how such ligands affect the reactivity of the MNC catalysts and their position on the volcano.

In this work, we explore the fundamental limitations in CO production with MNC materials, with M being either Fe or Ni. We build on our previously reported synthetic protocol that provides MNC materials with optimum utilization that allows us to maximize TOF and reach the highest values reported in the state-of-the-art (6.8 e^- $site^-$

^{1} s^{-1} at -0.59 V vs RHE).[21] The active site structure of the prepared catalysts is elucidated by means of X-ray absorption spectroscopy (XAS), the atomic dispersion by high angle annular dark field transmission electron microscopy (HAADF-TEM), and the effect of axial ligands in the binding energy of reaction intermediates is estimated by density functional theory calculations (DFT). Additionally, the stability of the catalyst is assessed through time-of-flight secondary ion mass spectrometry (TOF-SIMS) pre and post extended measurements. Finally, we compare the TOF of the best performing CO_2-to-CO catalysts in the literature, showing the existence of similar fundamental limitation for MNC catalyst as for metals.

Results and discussions

Nitrogen-doped carbon materials were prepared as recently shown by our group by pyrolysis of 2,4,6-Triaminopyrimidine (TAP) in the presence of $MgCl_2 \cdot 6H_2O$ at 900 ºC (**Figure 1**).[21] This process allows TAP to self-organize by hydrogen bonding between the amine groups and the water molecules of $MgCl_2 \cdot 6H_2O$ before polymerizing in a molten state.

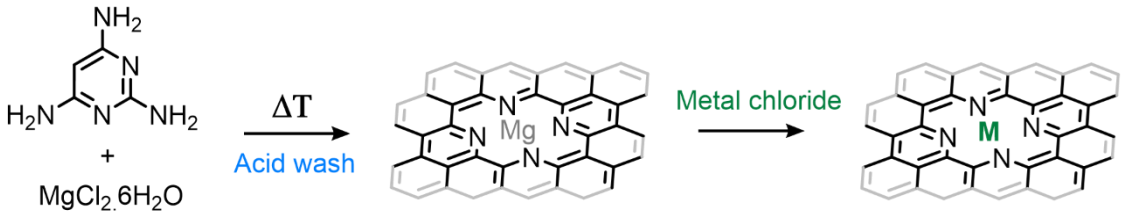

Figure 1. Synthetic pathway for the preparation of pyrolysed TAP 900 and the subsequent low temperature metal coordination. M represents Ni or Fe.

The pyrolysis of TAP in the presence of $MgCl_2 \cdot 6H_2O$ at 900 °C resulted, after acidic washing, in a highly porous nitrogen-doped carbon material with a Brauner-Emmett-Teller specific surface area ~3290 m^2 g^{-1} and bimodal pore size distribution centred at 0.8 and 2.1 nm. For further details regarding synthesis and characterization of the materials we would like to refer the reader to previous work.[21] Fe and Ni were coordinated in the N moieties of TAP 900 employing the method first reported by Fellinger and co-workers for O_2 reduction single atom catalysts.[31,32] TAP 900 reaction in methanol reflux with either $FeCl_2$ or $NiCl_2 \cdot 6H_2O$ led to 0.520 wt.% Fe and 0.265 wt.% Ni, respectively, determined by inductively coupled plasma mass spectrometry (ICP-MS) (**Figure 2a**). Fe is detected in TAP 900 and TAP 900@Ni, as well as trace amounts of Cu in all TAP materials, likely arising from the low purity TAP precursor. Meanwhile, XPS of the materials after metal coordination (**Figure 2b**, **Figure S1**) further confirms the metal loading. N1s chemical states shows a chemical contribution standing for N-metal coordination (arising from Mg in the case of bare TAP), as well as pyridinic, pyrrolic and graphitic, which remain consistent across the TAP materials. XRD patterns suggests the absence of large aggregated metallic nanoparticles, as no diffraction peaks are observed (**Figure S2**).

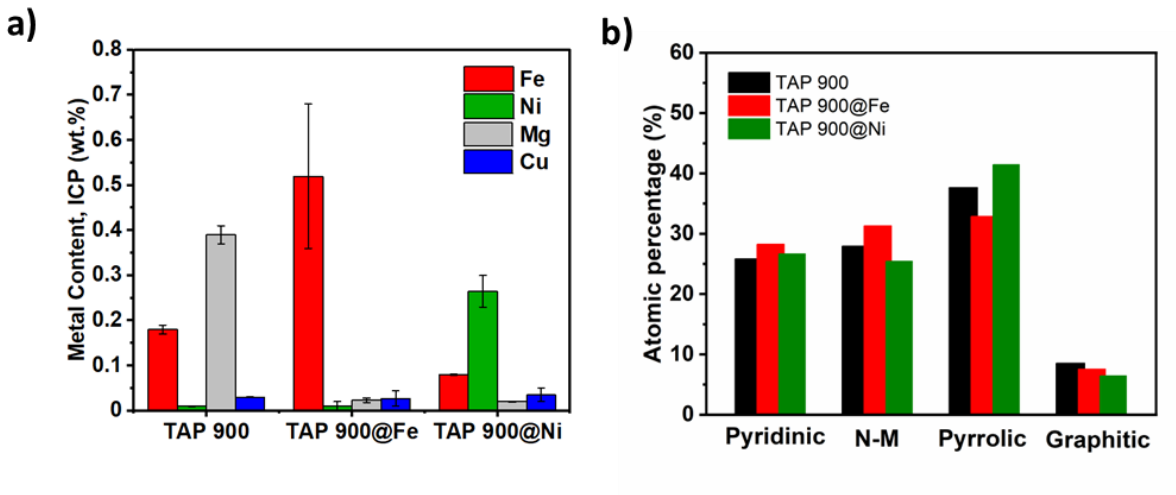

Figure 2. (a) Metal loadings in TAP 900@Fe and TAP 900@Ni calculated from ICP-MS (see experimental section at SI for further details on ICP-MS measurements). Two independent measurements for TAP 900 and TAP 900@Ni and four independent measurements for TAP 900@Fe were conducted, with the error bars representing the standard deviation. (b) N1s chemical states atomic percentage of TAP-derived materials before and after active metal coordination.

The atomic nature of both Fe and Ni was elucidated through HAADF-STEM. Both TAP 900@Fe and Ni are composed of atomically dispersed metals in a matrix of carbon and nitrogen, without visible presence of aggregates **(Figure 3**, **Figure S3**, **S4)**. Oxygen can be also observed owing to the remaining functionalities in the surface of the material (**Figure S5**). We employed Raman spectroscopy to elucidate the number of layers in our materials as shown recently by Mehmood *et al.* (**Supplementary Note 1**).[20] We observed that the number of carbon layers is approximated to be 1**,** which is expected for a high surface area catalyst (**Figure S6-S7**), and which suggests a very high accessibility of the N-coordinated metallic single atoms in a graphene-like layer.

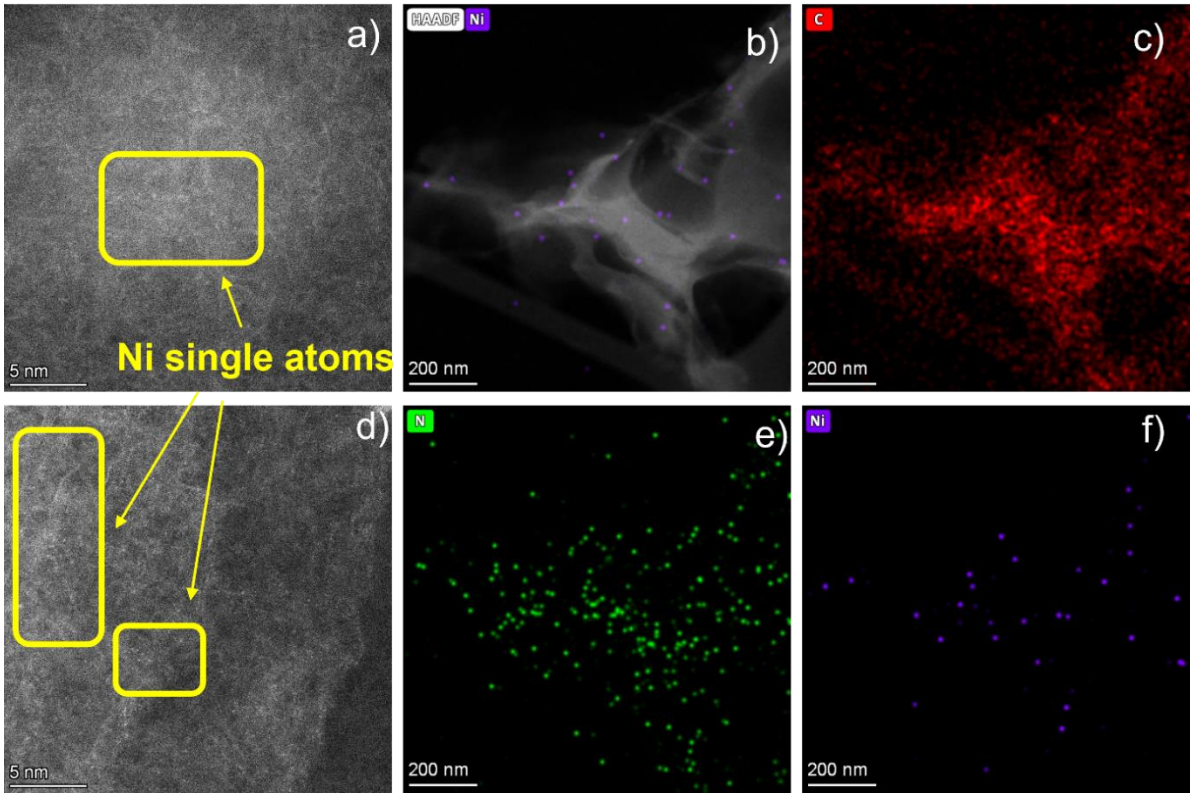

Figure 3. HAADF images (a, d) and EDX mapping (b, c, e, f) for C (red), N (green) and Ni (violet) for TAP 900@Ni pre-electrochemistry.

Cryo (5 K) X-band EPR was chosen to probe unpaired electrons within the catalyst (**Figure S8**). As shown in our previous work, TAP 900 shows a sharp g ~ 2 signal, most likely from organic radicals,[11] which may arise from defect states of the carbon support. The reduced g ~ 2 signal in TAP 900@Ni suggests the organic radicals are removed during the metalation and acid washing process with the slight background signal remaining arising from the EPR tube or resonator. Previous EPR studies on Ni have observed signals at g ~ 2.2, assigned to the $3dx^2$-y^2 orbital of Ni(I) species.[33,34] However, TAP 900@Ni does not exhibit any signal at g ~ 2.2, indicating that Ni (II) is the resting state in the as-synthesized TAP 900@Ni catalyst.

The coordination environment around TAP 900@Fe and Ni was further evaluated through *ex-situ* X-ray absorption measurements. As discussed in previous work, the first derivative of the normalised XANES in TAP 900@Fe indicates a structural distortion (broken D_{4h} symmetry) and the presence of a penta-coordinated Fe site.[35,36] Conversely, XANES spectra, in addition to EPR, of TAP 900@Ni showed that a +2 oxidation state is predominant for Ni, and owing to its electronic configuration it is not expected to display a penta-coordinated environment (**Figure 4c-d**). Only one prominent peak is observed at 1.55 Å in the Fourier transformed (FT) extended X-ray absorption fine structure (EXAFS) spectrum (**Figure S9a,b**), which is attributed to the M–N contribution. Moreover, no scattering peaks arising from M-M coordination are seen in TAP 900@M (where M = Ni or Fe). These results confirm the atomic distribution of Fe/Ni, consistent with the observations from STEM measurements as shown above. The low Ni content within TAP 900@Ni did not allow for an accurate EXAFS fitting, but Ni-N coordination is indirectly confirmed by time-of-flight secondary ion mass spectrometry (ToF-SIMS, discussed later). Meanwhile first-coordination EXAFS structural fitting was possible on TAP 900@Fe

(**Table S1**) which showed a coordination number (CN_{Fe-N}) ~5.6, indicating the presence of a mixture of FeN_5 and FeN_6 active sites, consistent with our previous report via low-temperature Mössbauer spectroscopy.[21]

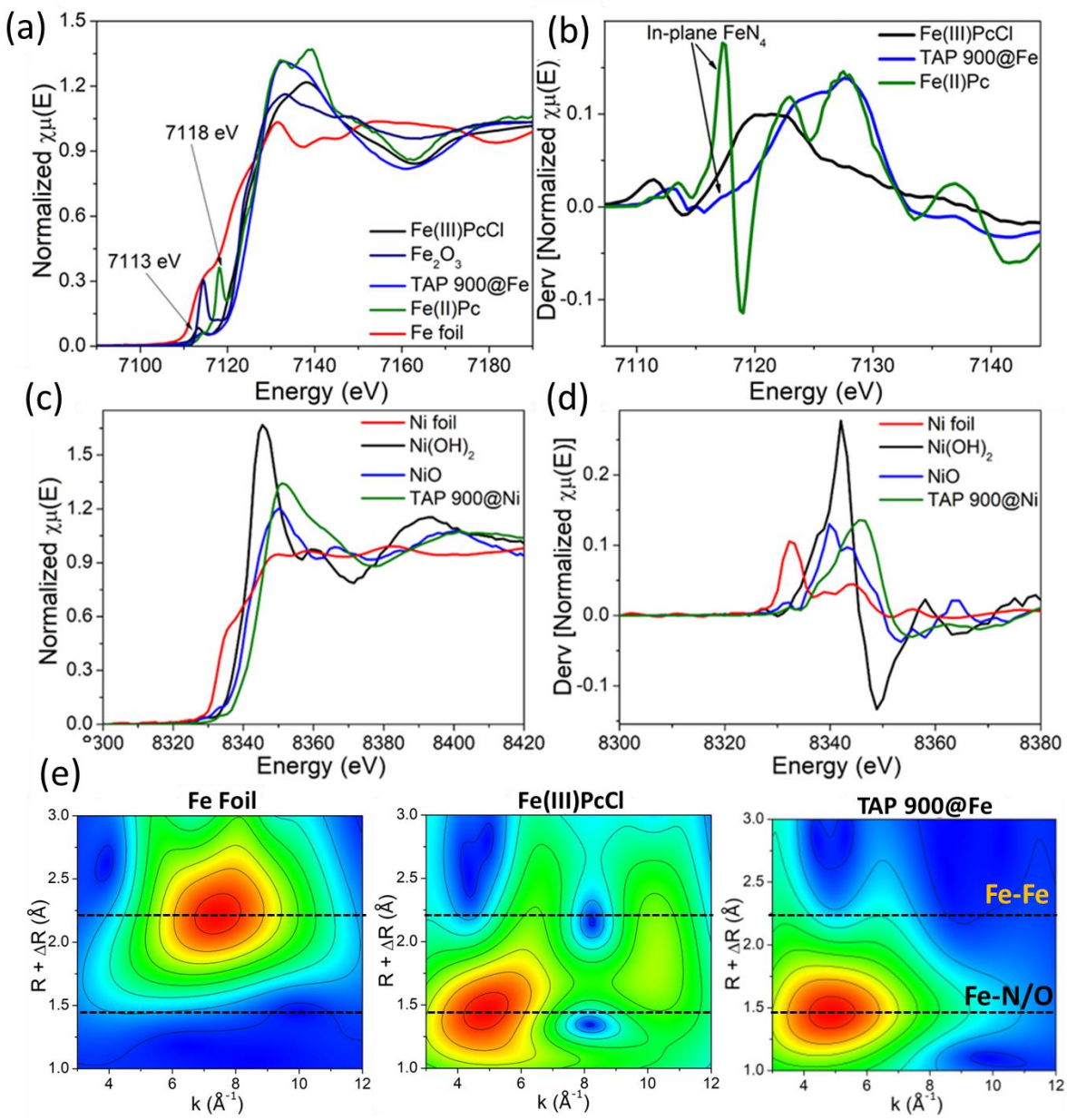

Figure 4. (a) Ex-situ XANES and (b) normalized first-derivative spectra of as received TAP 900@Fe compared with reference XANES spectra of Fe(II)Pc, Fe(III)PcCl, Fe_2O_3 and Fe-foil. (c) XANES and (d) normalized first-derivative spectra of TAP 900@Ni compared with reference XANES spectra of Ni foil, $Ni(OH)_2$ and NiO. € Wavelet transform of the k^2 weighted EXAFS data of Fe foil, Fe(III)PcCl and TAP 900@Fe. Dotted line represents the position of Fe-Fe and Fe-N/O radial bond distance.

Wavelet transform was employed to demonstrate the atomic positions of the Fe atom in the synthesized sample with respect to the Fe foil and Fe(III)PcCl references. As shown in **Figure 4e**, Fe foil has a strong signal at ~2.3 Å that can be assigned to the Fe-Fe bond distance, while Fe(III)PcCl has a strong wavelet signal at 1.4 Å implying the presence of shorter Fe-N/O bonds. TAP 900@Fe exhibits a similar wavelet signal to Fe(III)PcCl due to the presence of Fe-N bonds.

Aside from tuning the catalyst coordination, the wettability of the electrode is critical for improving the CO2RR microenvironment and optimising triple-phase interface of solid, liquid and gas.[37] Super hydrophilic electrode surfaces cause flooding of the GDE and flow-channel, leading to unwanted hydrogen evolution, whereas superhydrophobic surfaces may not allow for enough contact between the electrolyte and the electrocatalyst.[38] As a result, the coexistence of hydrophilic and hydrophobic conditions is considered as an ideal condition.[39] Water vapor adsorption measurement (obtained at 25 °C) on TAP 900 is compared to hydrophilic and hydrophobic carbons reported in previous literature in **Figure S10,**[9] which shows that the TAP 900 carbon-framework is relatively hydrophobic in nature, thus facilitating the CO2RR reaction.

The prepared materials were employed as electrocatalysts for the CO_2 reduction in 0.5 M $KHCO_3$. In an aqueous environment, CO_2 possesses a major mass-transport limitations due to its moderate solubility (33 mM at 1 atm and 25 °C). To circumvent this issue, we mixed the active catalyst with hydrophobic PTFE and used a customised electrochemical cell (**Figure S11**) to separate the gas flow channel and liquid compartment.[37] This ensured the formation of three-phase interface between gaseous CO_2, solid active catalyst, and the aqueous electrolyte. Thus, the working electrode was prepared by spray-coating an ink comprising active catalyst and PTFE to maintain a catalyst loading of 0.75 mg cm^{-2} on a carbon paper with an active geometric surface area of 1 cm^2. SEM image of the spray coated TAP 900@Ni electrode is shown in **Figure S12** which shows the flaky nature of the synthesized catalyst together with PTFE particles. Prior to the electrochemical testing, the surface of the electrode was preconditioned by conducting cyclic voltammetry measurements in the potential range of 0.1 to +0.6 V vs. RHE (**Figure S13**) with Ag/AgCl and 40% Pt/C (spray coated on carbon paper with 40 wt % loading of Pt) as a reference and counter electrode, respectively. Additionally, Fumasep FAA-3-50, an anion exchange membrane (AEM), was employed to separate the catholyte and anolyte compartments (see SI for more information regarding the AEM). Impedance spectroscopic measurements were used to calculate the uncompensated ohmic resistances, which yielded the iR-corrected potentials (see electrochemical measurement section of SI for details).

Chronoamperometric runs were conducted for 40 mins at each potential ranging from -0.3 V to -0.6 V vs. RHE. We could observe that with both TAP 900@Fe and TAP 900@Ni electrodes, the sum of FE_{CO} and FE_{H2} reached almost 100%, indicating the absence or negligible formation of other products. Selectivity towards CO varies depending on the choice of the transition metals (Fe or Ni). TAP 900@Fe showed good CO2RR activity at less negative potentials and approached a high CO selectivity (mean FE_{CO} = 93.5 $\pm$ 3.7 %) at -0.55 V vs RHE. In contrast, TAP 900@Ni exhibited low CO selectivity at less negative potentials and reached maximum CO selectivity (mean FE_{CO} = 95.3 $\pm$ 4.7 %) at -0.59 V. Bare TAP 900 showed very poor selectivity towards CO indicating the activity in TAP 900@M resulting predominantly from the M-N_x sites **(Figure 5a**). The partial current density of TAP 900@Fe and TAP 900@Ni to CO has been plotted and compared to some of the best reported catalysts (**Figure 5b**). TAP 900@Ni showed high stability as exemplified by the 10 h chronoamperometric test, where the FE remained >90 % with 98 % of the initial current for CO production and a stable current density of 15 mA cm^{-2} at -0.57 V vs RHE (**Figure 5c**). SEM images of pre- and post-measurement spray coated TAP 900@Ni (**Figure S14)** demonstrated that the morphology of the electrode surface remains unchanged.

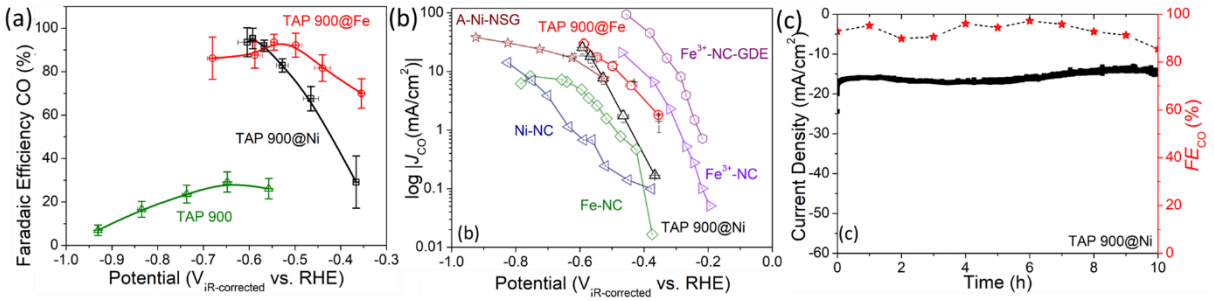

Figure 5. CO_2 reduction performance of TAP 900, TAP 900@Fe and TAP 900@Ni in 0.5 M $KHCO_3$. Three independent measurements were performed to calculate the error bar, representing the standard deviation. Chronoamperometric tests for calculating FE and partial current densities were conducted for 40 mins between -0.3 V to -0.6 V vs. RHE. (a) Faradaic efficiency of CO production, (b) Partial current densities adapted from previous literature (A-Ni-NSG,[40] Fe^{3+}-NC,[41] Fe^{3+}-NC-GDE,[41] Ni-NC,[10] Fe-NC[10]) and (c) Chronoamperometry curve and Faradaic efficiency of CO production by TAP 900@Ni at –0.57 V versus RHE.

Insights into the surface fragments of the materials were obtained through Time-of-flight Secondary Ion Mass Spectrometry (ToF-SIMS), which has emerged as a powerful tool to elucidate active site composition in single and dual atom electrocatalysts.[12,13,42] Here, ToF-SIMS was used to help confirm the NiN_xC_y moieties in TAP 900@Ni (**Figure S15**) and probe the stability of these moieties by measurement prior and post-chronoamperometry (post-CA) testing (45 mins at -0.55 V vs. RHE). TAP 900@Ni was recorded in negative polarity of SIMS due to the previously reported higher ionisation yields of NiN_xC_y fragments with the primary ion beam.[42] Prior to ToF-SIMS measurements the surface was lightly sputtered with an Ar beam to cleanse the surface of contaminants such as small organics. In contrast to other reports on similar materials,[43,44] we could not detect FeN_xC_y in TAP 900@Fe due to a combination of low FeN_xC_y ionisation yields and high-count organic species masking possible FeN_xC_y peaks.

Focussing on ToF-SIMS of TAP 900@Ni, confirmation of peak identification and correction is necessary since many peaks cannot be deconvoluted due to the equivalent masses of possible isotopic fragments. Peak identification and validation are discussed in **Supplementary Note 2**. Due to the low Ni content in TAP 900@Ni, many Ni ion fragments counts are low; therefore, focus is made on Ni fragments which exhibit clearly defined peaks in the mass spectrum. As mentioned earlier, EXAFS was not possible due to the low Ni content, however the identified fragments in **Figure 6** supports the identification of isolated Ni single atoms in N-doped C from combined HAADF-STEM and elemental mapping EDX. We found no detectable peaks in m/z values matching those of possible dual Ni atom fragments ($Ni_2N_xC_y^-$), confirming a purely single NiN_x atom nature of the TAP 900@Ni catalyst. Interestingly, in **Figure 6**, normalised counts are lower prior to electrochemistry for all Ni fragments identified, suggesting that under reaction conditions, more Ni sites are exposed over time, or species are introduced on the catalyst surface which enhance $NiN_xC_y^-$ fragment yield. The homogeneous dispersion of Ni fragments across the post-CA TAP 900@Ni is confirmed by imaging from ToF-SIMS (**Figure S16**).

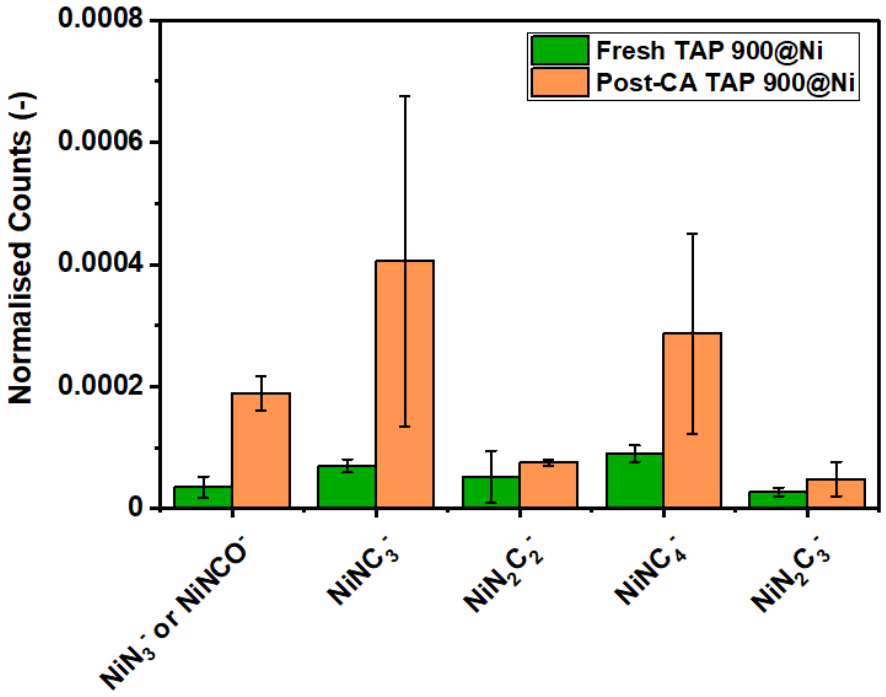

Figure 6. ToF-SIMS of Ni ion fragments pre- and post-chronoamperometry of TAP 900@Ni in the negative spectrum. Measurements were repeated five times in separate locations and corrected counts normalised to the total ion counts, with the error bars representing the standard deviation. To cleanse the catalyst surface, the samples were first non-interlaced sputtered with a 10 keV Ar^+ cluster ion beam at ~10 nA current, until reaching a dose density of 1×10^{15} ion cm^{-2}. For measurements a Bi_3^+ primary ion beam with 25 keV and 0.5 pA beam current was used for 25 mins.

Having understood the nature and stability of the active site, we then went on to quantify the number of active sites, which in turn allows us to accurately determine the turnover frequency (TOF), the number of product molecules produced or reactants consumed per unit time on a single active site. In a bulk or nanostructured catalyst, most of the active sites are inaccessible, therefore the CO2RR intermediate is adsorbed and interacts exclusively with the surface atoms/active sites during a catalytic process. This lowers the catalyst's atomic utilisation efficiency. However, due to their atomic dispersion in the carbon matrix, in theory MNCs could achieve 100% active site utilisation. In practice, MNC active sites are inaccessible due to a lack of porosity, particularly mesoporosity, therefore utilisation typically remain under 10%.[19] We determined the number of electrochemical active sites per cm^2 ($N_{Nitrite}$) by means of *in situ* electrochemical nitrite stripping experiments (**Figure S17**)[45] and compared it to the bulk active site density per cm^2 obtained by ICP (N_{ICP}) (**Eq. S4-S5**), to obtain the electrochemical active site utilisation efficiency ($Utilisation_{Nitrite/ICP}$) (**Eq. S6**).[46] For TAP 900@Fe and TAP 900@Ni, we obtain $N_{Nitrite}$ of 1.9 and 1.2×10^{19} sites cm^{-2} (**Table S2**). Considering measured N_{ICP}, we obtain $Utilisation_{Nitrite/ICP}$ of 45±14% and 59±6% for TAP 900@Fe and TAP 900@Ni, respectively (**Table S2**), the highest reported values to date for MNC catalysts. We would like to note that these values are based on nitrite stripping with a determined 5 e^- process,[47] however, if a 3e^- process to NH_2OH takes place, as previously suggested,[47,48] then $Utilisation_{Nitrite/ICP}$ for TAP 900@Fe and TAP 900@Ni would be 75±14% and 98±6%, respectively. The $Utilisation_{Nitrite/ICP}$ for TAP 900@Fe is likely lower due to inactive Fe contamination within TAP 900 (**Figure 2a**), which results in an increased Fe N_{ICP}. Nevertheless, these remarkably high values arise from the

combined micro- and meso-porosity of the TAP-derived materials, which allows for sufficient accessibility to the active sites as well as from the metal-coordination step, which hinders the aggregation and results in atomic dispersion within the C-N scaffold.

We define TOF_{min} and TOF_{max} as the TOF normalized with respect to the number of sites calculated using ICP and nitrite stripping (**Eq. S7-S8**), respectively, and a comparison is shown in **Figure S18**. State-of-the-art TOF are achieved for both TAP 900@Fe and TAP 900@Ni. TAP 900@Fe and TAP 900@Ni display TOFs of 4.9 and 6.8 e^- $site^{-1}$ s^{-1}, respectively, at -0.59 V vs. RHE (**Figure 7a**), which are over two orders of magnitude higher than the TOFs of other FeNCs, nanoporous Ag electrode (np-Ag)[46] and carbon black supported Au nanowires with a length of 500 nm (C-Au-500)[49]. We then compared the intrinsic activity in terms of TOF of different classes of catalysts that produce CO from CO_2. In **Figures S19** and **S20**, we show the TOF of Ni and Fe based MNC, respectively. We observe that the prepared materials show a TOF equal to the highest reporting materials of the same class, in particular TAP 900@Ni shows a similar TOF at -0.59 V vs RHE to that reported by Liu *et al*. with a Ni-CNT composite. In terms of FeNC materials, TAP 900@Fe shows the highest TOF at -0.59 V vs. RHE observed in the literature for FeNC materials.

To compare MNC materials with metal catalysts, we compare the catalytic activity in terms of number of CO_2 molecules reduced per site per second, for different metal-based catalysts including Cu and best-reported MNCs **(Figure 7b).** The fact that the plotted Cu catalysts exhibit identical intrinsic activity despite having different morphologies is particularly intriguing.[27,50] Although morphology and nanostructuring may enhance geometric current density, they have little impact on intrinsic activity.[27,51] It is also clear that the intrinsic activity of CO2RR to CO on Au-based and MNC catalysts are higher than on the surface of Cu metal-based samples. We attribute this to the fact that Cu binds *CO to enable 'beyond-CO' products, however, *CO in still case can also be considered a poison limiting the TOF of CO2RR. An optimum exists through the scaling of carbon intermediate, *via* an activation of CO_2 and desorption of *CO to CO.[23] Overall, TAP 900@Ni and TAP 900@Fe display the highest TOF, along with the reports by Gu *et al*.,[41] Choi *et al*.,[52] and Liu *et al*.,[53] showing as well substantially higher values than that of Cu-based materials.

Intriguingly, **Figure 7** shows a single fundamental limitation. The limitation can be simplified to the fact that CO_2 reduction is carbon chemistry; where carbon is activated and subsequently needs to get off the surface. Regardless of the exact CO_2 activation step, whether it is cation induced, electron induced or PCET to form *COOH, this study suggests that discussion of the absolute activation step is scientifically interesting, but only societally relevant if it allows research to overcome the barrier shown in the analysis of **Figure 7**.

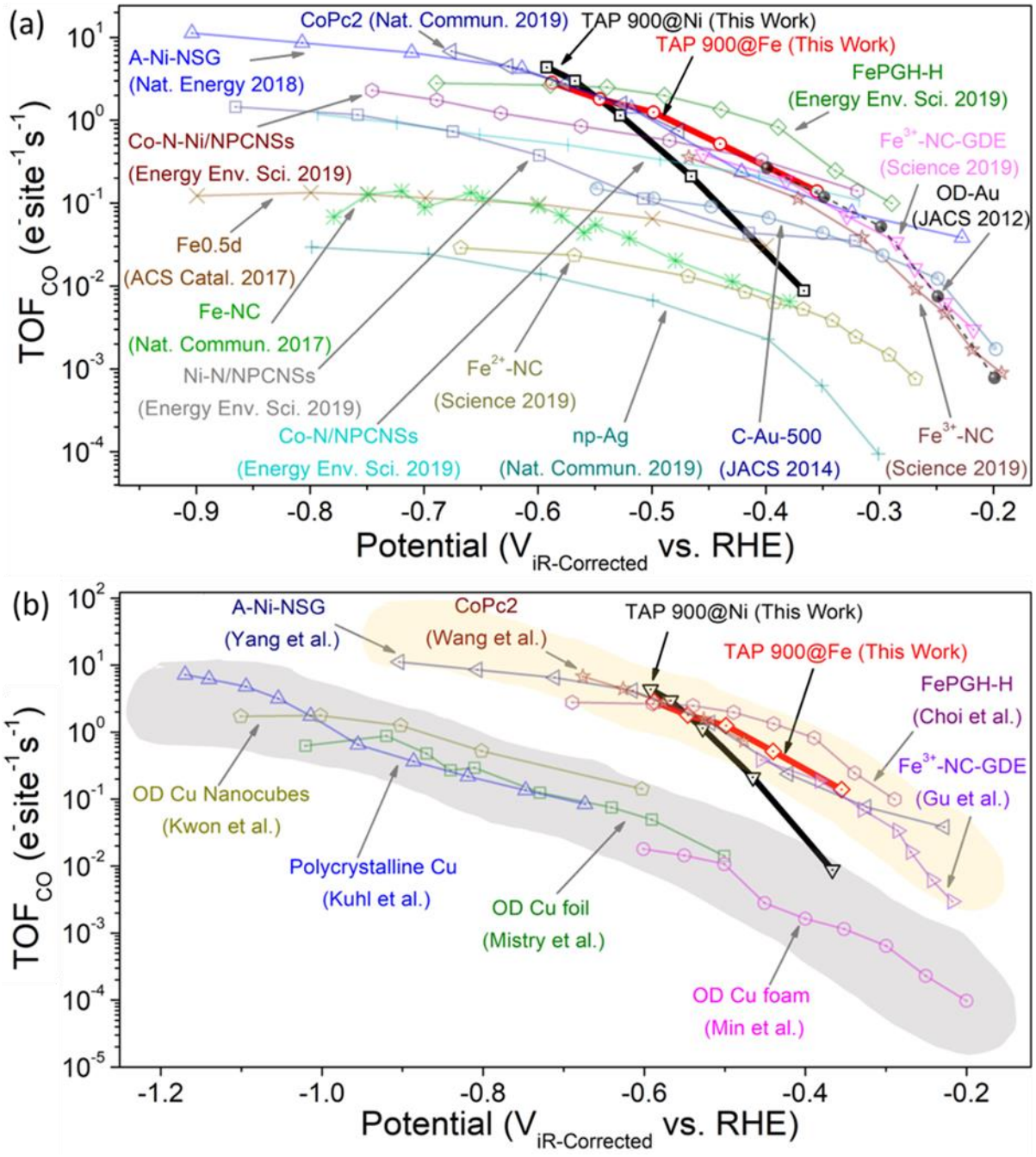

Figure 7. (a) Turnover frequency (TOF) of best-reported metal-doped carbon catalysts for CO_2 to CO conversion in aqueous salt electrolyte. A-Ni-NSG,[40] CoPc2,[54] TAP 900@Ni (this work), TAP 900@Fe (this work), FePGH-H,[52] Oxide-derived (OD) Au,[55] Fe^{2+}-NC,[41] Fe^{3+}-NC,[41] Fe^{3+}-NC-GDE,[41] C-Au-500,[49] np-Ag,[46] Co-N/NPCNSs,[56] Ni-N/NPCNSs,[56] Co-N-Ni/NPCNSs,[56] Fe-NC and Fe0.5d[16]. **(b)** Turnover frequency (TOF) of reported metal-doped carbon catalysts listing the number of CO_2 molecules reacted per site per second. A-Ni-NSG,[40] CoPc2,[54] TAP 900@Ni & TAP 900@Fe (this work), FePGH-H,[52] Fe^{3+}-NC-GDE,[41] OD Cu foam,[57] OD Cu foil,[58] polycrystalline Cu[59] and OD Cu nanocubes.[60]

To obtain insights into the catalytic activity of the prepared materials, DFT calculations were carried out. As CO_2 reduction to CO is a two proton-electron reaction, the simplistic picture is a Sabatier volcano as a function of one adsorption energy, in this case *COOH, which corresponds to the proton-electron coupled activated intermediate of CO_2. **Figure 8a** demonstrates this volcano with a strong binding leg (reaction: *COOH + (H^+ +

e^-) → CO(g) + H_2O) and weak (reaction: CO_2 + (H^+ + e^-) → *COOH) binding leg. Notably, such a construction is similar to the hydrogen evolution volcano (HER), which is also a two proton-electron reaction, where *H controls the reaction. However, the two proton-electron volcano is a too simplistic picture in the case of CO_2 to CO reduction, which needs to include three elements: i) activation of CO_2, ii) competition with HER and iii) desorption of CO. The first element is included directly by using the *COOH intermediate, while the two other elements can be added by using the scaling relations. Competition with HER (*H) is included by dashed vertical lines added from **Figure S21**, which show the scaling relationship between the adsorption energy of *COOH plotted against the *H adsorption energy for metal (111) and penta-coordinated FeN_4X surfaces. The scaling relationship, due to this difference in binding (on-top vs. hollow sites), gives two different intercepts for metals and MNCs. Finally, the CO desorption can also be included by using the scaling between *CO and *COOH from metals of (similar to that of Hansen et al.[23]), as the *CO and *COOH scaling on MNCs is poor. We are unaware if this is real or an artifact from the electronic structure on MN_4Cs. If we were to assume that the reaction is controlled by the adosprtion and desorption of *COOH, the most optimum catalyst would be at the peak of the volcano, where *COOH adsorption is thermoneutral. However, this is not the case, as competing reactions can occur: Hydrogen Evolution Reaction (HER), further reaction of CO or CO acting as a poisoning on the catalyst.[61] Hence, on the weak binding side, Au and Ag occupy an optimal position close to ΔG = 0 for CO (g) → *CO, showing that these catalysts need energy to activate CO_2, but are not limited by CO desorption. However, Au and Ag clearly do not sit at the top of the *COOH binding volcano, illustrating the fundamental constraint in CO_2 to CO catalysis. Interestingly, while Cu is closer to the top of the volcano, its CO2RR TOF is lower than the high TOF for OD-Au as seen in **Figure 7a**. This reflects that it is important not to have a CO2RR catalyst which is too reactive and hence is limited by binding *CO.

To understand the effect of the fifth axial coordination on the FeN_xC material, we computed the adsorption energy of *COOH on different catalyst structures containing different N-species (*NH_2, *NH_3, *CH_3, *Pyridine and *Pyrrole at axial position) on two types of nitrogen-doped carbon frameworks – namely 'Pyridinic-FeN_4' and 'Pyrrolic-FeN_4', indicating that Fe is coordinated to pyridinic or pyrrolic-N (at equatorial position). Optimized structures are shown in **Figure 8b** and **Figure S22**. The FeN_xC motifs without axial coordination are reactive and limited by *CO desorption. By adding the axial coordination, which forms a chemical bond to the Fe site, the site binds *COOH less strongly. The NH_2 bonded to Pyrrolic FeN_4 and Pyrrole bonded to pyrrolic-FeN_4 lies closer to the Au, implying that a nitrogen bond in the axial position could improve activity by not being limited by *CO desorption. Ideally, any catalyst close to the vertical dashed line of CO (g) → *CO should exhibit superior activity. Like most of best reported CO_2 to CO catalysts, TAP 900@Fe and Au have similar TOF as seen in **Figure 7a** and thus, we can assume they lie around ΔG = 0 line for CO (g) → *CO. Consequently, our data point towards the existence of a fundamental limitation – or celiing – that prevents the attainment of higher CO_2 to CO activity than Au towards; this limitation is due to the scaling relation between the stability of the activated form of CO_2 (whether it is *COOH or *CO2 stabilised by a cation) and *CO. To the best of our knowledge, there is no evidence that any solid electrocatalyst, including, the MNC catalyst we report therein, has not been subject to this scaling relation and exhibited better TOF.

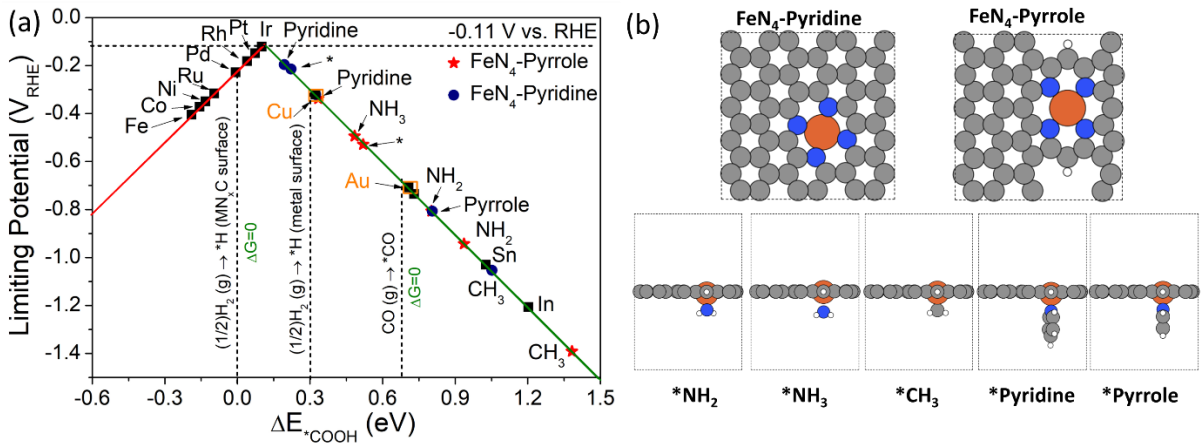

Figure 8. The limiting potential volcano for CO_2 reduction to CO on (a) metal (111) surface and FeN_4-X where X is the ligand attached. MN_4 adsorption data were extracted from the previous reference.[62] The red line represents that the reaction is limited by the strong binding of *COOH and the green line represents that the reaction is limited by the weak binding of COOH. The horizontal black line at -0.11 V_{RHE} represents the equilibrium potential. Vertical dashed lines represent the ΔG=0 for the respective reactions. ΔG=0 for HER is different for Metal and MN_4 surface while it is similar for *CO adsorption/desorption. (b) Structures of FeN_4-Pyridine and FeN_4-Pyrrole with different adsorbed molecules (*NH_2, *NH_3, *CH_3, *Pyridine and *Pyrrole) at an axial position.

Conclusions

In this work, we developed single atom MNC CO2RR catalysts through a decoupled synthesis approach that entailed the selective coordination of metal sites in highly porous N-doped carbon, leading to a record electrochemically active site utilisation. The high accessibility of the active sites enabled by the mesoporosity of the substrate as well as the presence of an axial ligand that favourably shifts the binding energy of reaction intermediates. These features enabled a CO_2 to CO electrocatalytic performance equal to the highest TOF in the literature value for MNC materials, equivalent, but not surpassing that of Au. Our experimental observation that the most active materials converge in terms of intrinsic activity supports the theoretical notion that scaling relations exists between the stability of the carbon-containing intermediates. Moving forwards, there are two routes to improving beyond the state-of-the art (a) finding compounds that preferentially accelerate the CO_2 activation step relative to *CO desorption, for instance by manipulating the spin state of MNC catalysts[63] (b) or emulating enzymes such as nitrogenase so that we engineer the catalysts to yield more energy rich C2+ products.[64,65]

Acknowledgements

S. C. S and J. B. contributed equally to this work. The authors acknowledge financial support from the Engineering and Physical Sciences Research Council (EPSRC) (EP/M0138/1, EP/M013812/1 and EP/S023259/1), the European Research Council (ERC) under the European Union's Horizon 2020 research and innovation programme (grant agreement no. 866402) and the National Research Council of Canada through the Materials for Clean Fuels Challenge Program. S. C. S. acknowledges Marie Skłodowska-Curie Fellowship

H2020-MSCA-IF-2019 (896637). A. P. thanks supports from the EPSRC Centre for Doctoral Training in the Advanced Characterisation of Materials (grant number EP/L015277/1), and the Imperial College London SPIN-Lab (equipment grant number: EP/P030548/1) with Dr. Irena Nevjestic (equipment grant number: EP/P030548/1) and Surface Analysis Lab with Dr. Sarah Fearn. Maria-Magdalena Titirici acknowledges the Royal Academy of Engineering Chair in Emerging Technologies Fellowship. A.B acknowledges support from the Carlsberg Foundation (grant number CF21-0114).

References

[1] H. J. Erick, L. Fengwang, O. Adnan, S. R. Armin, G. de A. F. Pelayo, L. Shijie, Z. Shuzhen, L. Mingchuan, W. Xue, L. Yanwei, X. Yi, B. Koen, M. R. Kai, D. Cao-Thang, S. David, S. E. H., *Science (80-.).* **2021**, *372*, 1074.

[2] A. Robb, A. Ozden, R. K. Miao, C. P. O'Brien, Y. Xu, C. M. Gabardo, X. Wang, N. Zhao, F. P. García de Arquer, E. H. Sargent, D. Sinton, *ACS Appl. Mater. Interfaces* **2022**, *14*, 4155.

[3] Y. Zhou, A. J. Martín, F. Dattila, S. Xi, N. López, J. Pérez-Ramírez, B. S. Yeo, *Nat. Catal.* **2022**, *5*, 545.

[4] E. Bertheussen, T. V Hogg, Y. Abghoui, A. K. Engstfeld, I. Chorkendorff, I. E. L. Stephens, *ACS Energy Lett.* **2018**, *3*, 634.

[5] X. Wang, P. Ou, A. Ozden, S.-F. Hung, J. Tam, C. M. Gabardo, J. Y. Howe, J. Sisler, K. Bertens, F. P. García de Arquer, R. K. Miao, C. P. O'Brien, Z. Wang, J. Abed, A. S. Rasouli, M. Sun, A. H. Ip, D. Sinton, E. H. Sargent, *Nat. Energy* **2022**, *7*, 170.

[6] A. Goyal, G. Marcandalli, V. A. Mints, M. T. M. Koper, *J. Am. Chem. Soc.* **2020**, *142*, 4154.

[7] C. Kim, T. Eom, M. S. Jee, H. Jung, H. Kim, B. K. Min, Y. J. Hwang, *ACS Catal.* **2017**, *7*, 779.

[8] Y. Hori, H. Wakebe, T. Tsukamoto, O. Koga, *Electrochim. Acta* **1994**, *39*, 1833.

[9] W. Ju, A. Bagger, G.-P. Hao, A. S. Varela, I. Sinev, V. Bon, B. Roldan Cuenya, S. Kaskel, J. Rossmeisl, P. Strasser, *Nat. Commun.* **2017**, *8*, 944.

[10] A. S. Varela, W. Ju, A. Bagger, P. Franco, J. Rossmeisl, P. Strasser, *ACS Catal.* **2019**, *9*, 7270.

[11] A. S. Varela, N. Ranjbar Sahraie, J. Steinberg, W. Ju, H.-S. Oh, P. Strasser, *Angew. Chemie Int. Ed.* **2015**, *54*, 10758.

[12] C. Jia, S. Li, Y. Zhao, R. K. Hocking, W. Ren, X. Chen, Z. Su, W. Yang, Y. Wang, S. Zheng, F. Pan, C. Zhao, *Adv. Funct. Mater.* **2021**, *31*, 2107072.

[13] A. Pedersen, J. Barrio, A. Li, R. Jervis, D. J. L. Brett, M. M. Titirici, I. E. L. Stephens, *Adv. Energy Mater.* **2022**, *12*, 2102715.

[14] H. Wan, Y. Jiao, A. Bagger, J. Rossmeisl, *ACS Catal.* **2021**, *11*, 533.

[15] E. González-Cervantes, A. A. Crisóstomo, A. Gutiérrez-Alejandre, A. S. Varela, *ChemCatChem* **2019**, *11*, 4854.

[16] T. N. Huan, N. Ranjbar, G. Rousse, M. Sougrati, A. Zitolo, V. Mougel, F. Jaouen, M. Fontecave, *ACS Catal.* **2017**, *7*, 1520.

[17] N. R. Sahraie, U. I. Kramm, J. Steinberg, Y. Zhang, A. Thomas, T. Reier, J.-P. Paraknowitsch, P. Strasser, *Nat. Commun.* **2015**, *6*, 8618.

[18] D. Malko, A. Kucernak, T. Lopes, *Nat. Commun.* **2016**, *7*, 1.

[19] M. Primbs, Y. Sun, A. Roy, D. Malko, A. Mehmood, M.-T. Sougrati, P.-Y. Blanchard, G. Granozzi, T. Kosmala, G. Daniel, P. Atanassov, J. Sharman, C. Durante, A. Kucernak, D. Jones, F. Jaouen, P. Strasser, *Energy Environ. Sci.* **2020**, *13*, 2480.

[20] A. Mehmood, M. Gong, F. Jaouen, A. Roy, A. Zitolo, A. Khan, M. Sougrati, M. Primbs, A. M. Bonastre, D. Fongalland, G. Drazic, P. Strasser, A. Kucernak, *Nat. Catal.* **2022**, *5*, 311.

[21] et. al. J. Barrio, A. Pedersen, S. C. Sarma, A. Bagger, M. Gong, S. Favero, C.-X. Zhao, R. Garcia-Serres, A. Y. Li, *ChemRxiv* **2022**, DOI https://doi.org/10.26434/chemrxiv-2022-8bt8r.

[22] S. Vijay, W. Ju, S. Brückner, S.-C. Tsang, P. Strasser, K. Chan, *Nat. Catal.* **2021**, *4*, 1024.

[23] H. A. Hansen, J. B. Varley, A. A. Peterson, J. K. Nørskov, *J. Phys. Chem. Lett.* **2013**, *4*, 388.

[24] A. A. Peterson, F. Abild-Pedersen, F. Studt, J. Rossmeisl, J. K. Nørskov, *Energy Environ. Sci.* **2010**, *3*, 1311.

[25] M. C. O. Monteiro, F. Dattila, B. Hagedoorn, R. García-Muelas, N. López, M. T. M. Koper, *Nat. Catal.* **2021**, *4*, 654.

[26] A. S. Varela, M. Kroschel, N. D. Leonard, W. Ju, J. Steinberg, A. Bagger, J. Rossmeisl, P. Strasser, *ACS Energy Lett.* **2018**, *3*, 812.

[27] S. Nitopi, E. Bertheussen, S. B. Scott, X. Liu, A. K. Engstfeld, S. Horch, B. Seger, I. E. L. Stephens, K. Chan, C. Hahn, J. K. Nørskov, T. F. Jaramillo, I. Chorkendorff, *Chem. Rev.* **2019**, *119*, 7610.

[28] J. Tuo, Y. Zhu, H. Jiang, J. Shen, C. Li, *ChemElectroChem* **2020**, *7*, 4767.

[29] K. Jiang, S. Siahrostami, A. J. Akey, Y. Li, Z. Lu, J. Lattimer, Y. Hu, C. Stokes, M. Gangishetty, G. Chen, Y. Zhou, W. Hill, W.-B. Cai, D. Bell, K. Chan, J. K. Nørskov, Y. Cui, H. Wang, *Chem* **2017**, *3*, 950.

[30] H. Zhang, J. Li, S. Xi, Y. Du, X. Hai, J. Wang, H. Xu, G. Wu, J. Zhang, J. Lu, J. Wang, *Angew. Chemie Int. Ed.* **2019**, *58*, 14871.

[31] J. Barrio, A. Pedersen, J. Feng, S. C. Sarma, M. Wang, A. Y. Li, H. Yadegari, H. Luo, M. P. Ryan, M.-M. Titirici, I. E. L. Stephens, *J. Mater. Chem. A* **2022**, *10*, 6023.

[32] A. Mehmood, J. Pampel, G. Ali, H. Y. Ha, F. Ruiz-Zepeda, T.-P. Fellinger, *Adv. Energy Mater.* **2018**, *8*, 1701771.

[33] M. Tavakkoli, T. Kallio, O. Reynaud, A. G. Nasibulin, C. Johans, J. Sainio, H. Jiang, E. I. Kauppinen, K. Laasonen, *Angew. Chemie Int. Ed.* **2015**, *54*, 4535.

[34] R. Bonetto, F. Crisanti, A. Sartorel, *ACS Omega* **2020**, *5*, 21309.

[35] J. Li, S. Ghoshal, W. Liang, M.-T. Sougrati, F. Jaouen, B. Halevi, S. McKinney, G. McCool, C. Ma, X. Yuan, Z.-F. Ma, S. Mukerjee, Q. Jia, *Energy Environ. Sci.* **2016**, *9*, 2418.

[36] R. Cao, R. Thapa, H. Kim, X. Xu, M. Gyu Kim, Q. Li, N. Park, M. Liu, J. Cho, *Nat. Commun.* **2013**, *4*, 2076.

[37] Z. Xing, L. Hu, D. S. Ripatti, X. Hu, X. Feng, *Nat. Commun.* **2021**, *12*, 136.

[38] K. Yang, R. Kas, W. A. Smith, T. Burdyny, *ACS Energy Lett.* **2021**, *6*, 33.

[39] H. Rabiee, L. Ge, J. Zhao, X. Zhang, M. Li, S. Hu, S. Smart, T. E. Rufford, Z. Zhu, H. Wang, Z. Yuan, *Appl. Catal. B Environ.* **2022**, *310*, 121362.

[40] H. Bin Yang, S.-F. Hung, S. Liu, K. Yuan, S. Miao, L. Zhang, X. Huang, H.-Y. Wang, W. Cai, R. Chen, J. Gao, X. Yang, W. Chen, Y. Huang, H. M. Chen, C. M. Li, T. Zhang, B. Liu, *Nat. Energy* **2018**, *3*,

140.

[41] G. Jun, H. Chia-Shuo, B. Lichen, C. H. Ming, H. Xile, *Science (80-.).* **2019**, *364*, 1091.

[42] D. M. Koshy, A. T. Landers, D. A. Cullen, A. V Ievlev, H. M. Meyer III, C. Hahn, Z. Bao, T. F. Jaramillo, *Adv. Energy Mater.* **2020**, *10*, 2001836.

[43] M. Lefèvre, J. P. Dodelet, P. Bertrand, *J. Phys. Chem. B* **2000**, *104*, 11238.

[44] M. Lefèvre, J. P. Dodelet, P. Bertrand, *J. Phys. Chem. B* **2002**, *106*, 8705.

[45] D. Malko, A. Kucernak, T. Lopes, *Nat. Commun.* **2016**, *7*, 13285.

[46] Q. Lu, J. Rosen, Y. Zhou, G. S. Hutchings, Y. C. Kimmel, J. G. Chen, F. Jiao, *Nat. Commun.* **2014**, *5*, 3242.

[47] D. Malko, A. Kucernak, T. Lopes, *J. Am. Chem. Soc.* **2016**, *138*, 16056.

[48] D. H. Kim, S. Ringe, H. Kim, S. Kim, B. Kim, G. Bae, H.-S. Oh, F. Jaouen, W. Kim, H. Kim, C. H. Choi, *Nat. Commun.* **2021**, *12*, 1856.

[49] W. Zhu, Y.-J. Zhang, H. Zhang, H. Lv, Q. Li, R. Michalsky, A. A. Peterson, S. Sun, *J. Am. Chem. Soc.* **2014**, *136*, 16132.

[50] L. Wang, S. Nitopi, A. B. Wong, J. L. Snider, A. C. Nielander, C. G. Morales-Guio, M. Orazov, D. C. Higgins, C. Hahn, T. F. Jaramillo, *Nat. Catal.* **2019**, *2*, 702.

[51] K. Chan, *Nat. Commun.* **2020**, *11*, 5954.

[52] J. Choi, J. Kim, P. Wagner, S. Gambhir, R. Jalili, S. Byun, S. Sayyar, Y. M. Lee, D. R. MacFarlane, G. G. Wallace, D. L. Officer, *Energy Environ. Sci.* **2019**, *12*, 747.

[53] S. Liu, H. Bin Yang, S.-F. Hung, J. Ding, W. Cai, L. Liu, J. Gao, X. Li, X. Ren, Z. Kuang, Y. Huang, T. Zhang, B. Liu, *Angew. Chemie Int. Ed.* **2020**, *59*, 798.

[54] M. Wang, K. Torbensen, D. Salvatore, S. Ren, D. Joulié, F. Dumoulin, D. Mendoza, B. Lassalle-Kaiser, U. Işci, C. P. Berlinguette, M. Robert, *Nat. Commun.* **2019**, *10*, DOI 10.1038/s41467-019-11542-w.

[55] Y. Chen, C. W. Li, M. W. Kanan, *J. Am. Chem. Soc.* **2012**, *134*, 19969.

[56] J. Pei, T. Wang, R. Sui, X. Zhang, D. Zhou, F. Qin, X. Zhao, Q. Liu, W. Yan, J. Dong, L. Zheng, A. Li, J. Mao, W. Zhu, W. Chen, Z. Zhuang, *Energy Environ. Sci.* **2021**, *14*, 3019.

[57] S. Min, X. Yang, A.-Y. Lu, C.-C. Tseng, M. N. Hedhili, L.-J. Li, K.-W. Huang, *Nano Energy* **2016**, *27*, 121.

[58] H. Mistry, A. S. Varela, C. S. Bonifacio, I. Zegkinoglou, I. Sinev, Y.-W. Choi, K. Kisslinger, E. A. Stach, J. C. Yang, P. Strasser, B. R. Cuenya, *Nat. Commun.* **2016**, *7*, 12945.

[59] K. P. Kuhl, E. R. Cave, D. N. Abram, T. F. Jaramillo, *Energy Environ. Sci.* **2012**, *5*, 7050.

[60] Y. Kwon, Y. Lum, E. L. Clark, J. W. Ager, A. T. Bell, *ChemElectroChem* **2016**, *3*, 1012.

[61] N. Leonard, W. Ju, I. Sinev, J. Steinberg, F. Luo, A. S. Varela, B. Roldan Cuenya, P. Strasser, *Chem. Sci.* **2018**, *9*, 5064.

[62] A. Bagger, W. Ju, A. S. Varela, P. Strasser, J. Rossmeisl, *Catal. Today* **2017**, *288*, 74.

[63] Y. Liang, K. Banjac, K. Martin, N. Zigon, S. Lee, N. Vanthuyne, F. A. Garcés-Pineda, J. R. Galán-Mascarós, X. Hu, N. Avarvari, M. Lingenfelder, *Nat. Commun.* **2022**, *13*, 3356.

[64] I. E. L. Stephens, K. Chan, A. Bagger, S. W. Boettcher, J. Bonin, E. Boutin, A. K. Buckley, R. Buonsanti, E. R. Cave, X. Chang, S. W. Chee, A. H. M. da Silva, P. de Luna, O. Einsle, B. Endrődi, M. Escudero-Escribano, J. V Ferreira de Araujo, M. C. Figueiredo, C. Hahn, K. U. Hansen, S. Haussener,

S. Hunegnaw, Z. Huo, Y. J. Hwang, C. Janáky, B. S. Jayathilake, F. Jiao, Z. P. Jovanov, P. Karimi, M. T. M. Koper, K. P. Kuhl, W. H. Lee, Z. Liang, X. Liu, S. Ma, M. Ma, H.-S. Oh, M. Robert, B. R. Cuenya, J. Rossmeisl, C. Roy, M. P. Ryan, E. H. Sargent, P. Sebastián-Pascual, B. Seger, L. Steier, P. Strasser, A. S. Varela, R. E. Vos, X. Wang, B. Xu, H. Yadegari, Y. Zhou, *J. Phys. Energy* **2022**, *4*, 42003.

[65] J. Barrio, A. Pedersen, S. Favero, H. Luo, M. Wang, S. C. Sarma, J. Feng, L. T. T. Ngoc, S. Kellner, A. Y. Li, A. B. Jorge Sobrido, M.-M. Titirici, *Chem. Rev.* **2022**, DOI 10.1021/acs.chemrev.2c00429.

TOC: